High-resolution awake mouse fMRI at 14 Tesla

David Hike[1*], Xiaochen Liu[1*], Zeping Xie[1], Bei Zhang[1], Sangcheon Choi[1], Xiaoqing Alice Zhou[1], Andy Liu[1,2], Alyssa Murstein[1,2], Yuanyuan Jiang[1], Anna Devor[1,3], Xin Yu[1]

Author Affiliations:

[1]Athinoula A. Martinos Center for Biomedical Imaging, Department of Radiology, Harvard Medical School, Massachusetts General Hospital, 149 Thirteenth Street, Charlestown, Massachusetts, USA 02129

[2] Graduate program in Neuroscience, Boston University, Commonwealth Ave, Boston, Massachusetts, USA, 02215

[3] Department of Biomedical Engineering, Boston University, 610 Commonwealth Avenue, Boston, Massachusetts, USA, 02215

* Co-first authors contribute equally to this work.

Corresponding Author:

Xin Yu, Ph.D. 149 13th. Street, Charlestown, Massachusetts, USA, 02129

Email: XYU9@mgh.harvard.edu

Phone: 617-643-4883

Author Contributions:

DH, XL, XY designed the research. DH, XL, ZX, BZ, AL, XY performed the research. DH, XL, SC, XAZ, AM, YJ analyzed data. ZX, XAZ performed surgeries. DH, BZ, AL, AM built coils. DH, XL, BZ, AL designed animal cradle. DH, XL, AD, XY wrote the paper.

Competing Interest Statement:

MRIBOT LLC. is a spinoff company co-founded by XY

All other authors declare no competing interests related to this work.

Classification:

Biological Sciences: Neuroscience

Keywords: Awake Mouse, fMRI, BOLD, prediction, visual stimulation, vibrissa Stimulation,

Abstract

High-resolution awake mouse fMRI remains challenging despite extensive efforts to address motion-induced artifacts and stress. This study introduces an implantable radiofrequency (RF) surface coil design that minimizes image distortion caused by the air/tissue interface of mouse brains while simultaneously serving as a headpost for fixation during scanning. Using a 14T scanner, high-resolution fMRI enabled brain-wide functional mapping of visual and vibrissa stimulation at 100x100x200μm resolution with a 2s per frame sampling rate. Besides activated ascending visual and vibrissa pathways, robust BOLD responses were detected in the anterior cingulate cortex upon visual stimulation and spread through the ventral retrosplenial area (VRA) with vibrissa air-puff stimulation, demonstrating higher-order sensory processing in association cortices of awake mice. In particular, the rapid hemodynamic responses in VRA upon vibrissa stimulation showed a strong correlation with the hippocampus, thalamus, and prefrontal cortical areas. Cross-correlation analysis with designated VRA responses revealed early positive BOLD signals at the contralateral barrel cortex (BC) occurring 2 seconds prior to the air-puff in awake mice with repetitive stimulation, which was not detectable with the randomized stimulation paradigm. This early BC activation indicated learned anticipation through the vibrissa system and association cortices in awake mice under continuous training of repetitive air-puff stimulation. This work establishes a high-resolution awake mouse fMRI platform, enabling brain-wide functional mapping of sensory signal processing in higher association cortical areas.

Significance Statement

This awake mouse fMRI platform was developed by implementing an advanced implantable radiofrequency (RF) coil scheme, which simultaneously served as a headpost to secure the mouse head during scanning. The ultra-high spatial resolution (100x100x200μm) BOLD fMRI enabled the brain-wide mapping of activated visual and vibrissa systems during sensory stimulation in awake mice, including association cortices, e.g. anterior cingulate cortex and retrosplenial cortex, for high order sensory processing. Also, the activation of barrel cortex at 2 s prior to the air-puff indicated a learned anticipation of awake mice under continuous training of the repetitive vibrissa stimulation.

Introduction

Functional Magnetic Resonance Imaging (fMRI) indirectly measures brain activity via MRI contrast associated with endogenous blood oxygen level dependent (BOLD) signals(1–3). The BOLD contrast was first described by Pauling and Coryell in 1936(4), but it had not been utilized in anesthetized rodent MRI until 1990(1, 2). The power of BOLD-fMRI was later revealed in human brain functional mapping(5–7) and has revolutionized cognitive neuroscience. In contrast to human studies, preclinical fMRI has played a crucial role in method development and validation(3, 8–14). fMRI of anesthetized rodents reduces confounding artifacts due to motion and detects robust BOLD or Cerebral Blood Volume (CBV) signals under various anesthetics(15–29). Recently, the bridging power of preclinical fMRI for basic mechanistic and translational studies has been further exploited given the combination of rodent fMRI with genetic modification tools (e.g., optogenetics, chemogenetics, and genetically encoded biosensors)(8, 30–43). Among the many efforts in anesthetized rodent fMRI, mouse fMRI set a foundation for mechanistic multi-modal imaging given its global mapping scheme in genetic modification models(16, 19, 44, 45), as well as the ability to perform viral transfections to circuit- or cellular-specific targets in transgenic models. However, anesthetic treatment alters brain function during fMRI, preventing accurate interpretation of brain functional changes in awake states(15, 20, 23, 25, 26, 46–52).

Awake mouse fMRI presents itself to provide the most relevant brain functional mapping information for translational cross-scale brain dynamic studies. Awake mouse fMRI methodology has been well investigated(10, 47, 53–59) to solve the ongoing challenges of motion-induced artifacts and potential stress-related issues caused by loud noises and micro-vibrations during scanning(46, 47, 54, 56, 60–63). Previous work has demonstrated that well-planned training procedures could acclimate awake mice during scanning(56, 58, 60–62, 64–66). One ongoing challenge of awake mouse fMRI is to provide reproducible and high-quality brain functional images with sufficient spatiotemporal resolution and signal-to-noise ratio (SNR) to distinguish functional nuclei of mouse brains of only a few hundred microns. Since increasing spatiotemporal resolution leads to a reduction in SNR of the images, accessing the highest field MRI available, as well as maximizing the efficiency of the Radio Frequency (RF) transceiver signal is critical. Although cryoprobes have been well implemented to boost SNR, construction limitations of the superconducting environment constrain the usable space and flexibility to accommodate other imaging/recording modalities(13, 67–72). Implantable coils have been used in animal imaging for

over three decades(12, 73–79). Their use gained popularity due to higher SNR and reduction of susceptibility artifacts. The main limitation of implantable coils is the need to surgically implant these coils, adding a degree of invasiveness that MRI usually avoids. However, for typical awake mouse neuroimaging studies, surgical procedures to provide a head-fixation apparatus are routinely practiced. Replacing the conventional head-post for immobilization of the head with an implantable RF coil is critical for achieving high-resolution awake mouse fMRI using ultra-high field MRI, e.g., 14T.

In this present study, we established an awake mouse fMRI platform by implementing an implantable RF surface coil that is permanently affixed to the head and can simultaneously function as a head post for fixation during scanning to minimize animal motion. This setup allowed us to acquire images with a spatial resolution of 100µm in-plane and 200µm slice thickness. This unique implantable RF coil/headpost scheme simplified the awake mouse training and conditioning during imaging. It also helped reduce stress and improve B_0 homogeneity, as well as effectively eliminate any motion-related loading changes causing B_1 variability. Here we successfully mapped activated visual and vibrissa pathways and detected robust BOLD responses in the higher-order association cortices, e.g., Anterior Cingulate Area (ACA) with visual stimulation and Ventral Retrosplenial Area (VRA) with vibrissa stimulation in awake mice. Interestingly, the repetitive vibrissa stimulation paradigm in awake mice has enabled us to detect potential anticipatory learning predicting the onset of stimulation. Our work is a fundamental step towards combining high-resolution fMRI with other modalities to simultaneously record neuronal and microvascular signals throughout brain-wide circuity in awake mice.

Results

Development and efficiency validation of implantable RF coils to boost SNR

We have developed an implantable RF coil which effectively boosted the SNR in ultra-high field MRI. Here we compared two prototypes: a simple single loop coil design and a "figure 8" coil design and scanned to check SNR over anatomical data in anesthetized mice at 9.4T and 14T. **Figure 1** shows representative examples of two prototypes of RF coils (**Figure 1A, B**). The acquired SNR values for each prototype design were shown in figure **1C**. Here, we used a commercial 4 phase-array coil (400MHz for 9.4T) as a control to be compared with the implantable RF coils. The single loop implantable coils improved SNR 100% over the commercial option while

the figure 8 style showed a ~5x increase at 9.4T. Moving up to 14T, the SNR improvements increased proportionally as a factor of field strength(80). This improved SNR allows the high spatial resolution fMRI studies of awake mice.

Awake mouse fMRI with visual stimulation

The RF coil was implanted on the mouse skull to serve as an attachment for head fixation for awake mouse fMRI at 14T (**Figure 2A**). The awake mouse fMRI setup was designed using a 3D printed cradle with an incorporated sliding track to enable the printed circuit board (PCB) chip mounted on the mouse head to slide through the cradle. The PCB chip was then fixed in place at the end of the cradle using friction screws (**Supp Movie 1**). Once the mouse was fixed in the animal cradle, either a mirror or air tube was positioned for pupillometry recording or vibrissa stimulation, respectively. Additionally, an MRI-compatible camera was set up to record the pupil dynamic changes and whisking behavior of awake mice during scanning. One key feature of the awake mouse fMRI setup is the plug and play capability for scanning.

This awake mouse fMRI setup enabled high-resolution echo planar imaging (EPI) data acquisition at 100x100x200um spatial resolution with a 2s effective repetition time (TR). The EPI-based T2* images acquired from head-fixed awake mice show little air-tissue interface-induced image distortion with the same spatial resolution as anatomical images (**Figure 2C, D**). The motion artifacts were detected in some time points of the fMRI time course, presenting large EPI image distortions (**Figure 3E, Supp Movie 2**), which can be removed using a censoring function during data analysis (**Supp Figure 1**,). These results have shown that the multi-slice 2D EPI enables brain-wide functional mapping of awake mice.

To map the brain function of awake mice with this high-resolution fMRI method, we first introduced a visual stimulation paradigm. Based on the block-design regression analysis, we have detected robust BOLD responses. **Figure 3** showed the brain-wide function maps using the visual stimulation paradigm, with activated areas highlighted along the visual pathways. These areas included the visual cortex (VC), superior colliculus (SC), lateral geniculate nucleus (LGN), and association cortex in the anterior cingulate area (ACA). The ROI-specific localization was well characterized based on the overlapped brain atlas and functional maps (**Figure 3C**). **Figure 3B** shows the ROI-based time courses, demonstrating robust BOLD responses detected in awake mice.

Awake mouse fMRI with vibrissa stimulation

In contrast to the visual sensation, awake mice may flinch due to the sudden physical vibrissa stimulation causing severe motion artifacts during scanning. Prolonged training was needed to reduce motion artifacts during air-puff stimulation as shown in **Supp Movie 2**, allowing for high-resolution fMRI of awake mice. **Figure 4** showed the activated barrel cortex (BC) and ventroposterior medial nucleus (VPM) related to stimulation of the contralateral whisker pad (time courses in **Figure 4C**, **Supp Figure 2**). Brain-wide functional maps also showed activation in the motor cortex and a small portion of the ipsilateral BC. These results demonstrated the importance of distinguishing BOLD activation between external stimulation and voluntary movements while also confirming the feasibility to map brain-wide brain activations in awake behaving mice with 14T fMRI.

Prediction-related barrel cortical activity to patterned air-puff in awake mice

An interesting observation from the vibrissa stimulation was the activated VRA. In contrast to the typical duration of hemodynamic responses observed in the BC and VPM, the VRA only showed brief responses to air puff, presenting a good landmark for studying higher level processing of vibrissa sensation. Voxel-wise cross correlation analysis was performed based on the VRA-specific fMRI dynamic changes. At a zero time shift (map developed from peak BOLD response), the VRA is strongly correlated with the hippocampus, cingulate cortex, and central thalamic regions (**Figure 5A**). Nevertheless, at a -6s time shift (i.e., 2s before stimulation onset), stronger correlation was observed at the contralateral BC, indicating anticipation of the repetitive air-puff in the block design (**Figure 5A**). To validate that this early BC activation was caused by learned anticipation of the time-fixed repetitive air-puff stimulation, we also analyzed the VRA-specific cross correlation in a control group using a randomized stimulation paradigm. Although VRA remained strongly coupled with the other association cortices and subcortical regions at the zero time shift, no correlation was observed from the contralateral BC at the -6s time shift (**Figures 5 B**). The fMRI time course analysis from the contralateral BC also showed increased BOLD responses before the air-puff in the block design group, but not the randomized control group (**Figure 5C**). Quantitative analysis showed a significantly higher BOLD signal two seconds before the air puff stimulation in the standard block design group compared with the randomized group

(**Figure 5D**). It should be noted that VRA responses between the two groups were similar, further confirming the anticipation-related early BC activation to repetitive air-puff stimulation.

Discussion

In this study, we designed and implemented implantable RF coils for awake mouse fMRI, which also served as a headpost for head fixation during data acquisition. Our design, based on previously published cable-free (inductive) RF coils(79), offered an easier pre-scan setup by eliminating the need to localize and secure the pickup coil for inductive coupling optimization. And while this current design showed reduced freedom for animal movement, implanted coils offer a more stable sample loading and reduce the B_0 offset when compared to the previous version. This was also true when comparing to conventional RF coils as the motion of the animal would alter the loading and cause B_1 field variability during fMRI scanning.

Technical considerations with awake mouse fMRI at 14T

A few important factors should be considered to improve data quality using the implanted RF coils described in the present study. The first one is animal motion. As this design was used for awake and minimally restrained animals, the animals would eventually move to adjust themselves (scratching, grooming, teeth grinding, etc.) during the scan. This will affect B_0 homogeneity and can cause ghosting if severe enough. This can be minimized through acclimation training. Other studies have animal restraint mechanisms that seek to restrain the body of the animal(46, 47, 53, 58) but can cause unwanted stress which has the potential to affect the desired fMRI signals. The head-fixed mice using implanted RF coils allow free body movements, which has the downside of causing artifacts but ultimately limited stress. Furthermore, B_1 variability was present through motion as well due to the current design of the coil. As the RF circuit chip sits above the animal's neck, body movement could alter the loading of the circuit, inducing B_1 artifacts through lifting or dropping the body towards or away from the circuit chip. Again, these artifacts could be minimized through proper training and stress reduction which was well accomplished through the design and training method(60). Furthermore, mice have a thin skull, which leads to the air-tissue interface being a non-negligible factor at ultra-high fields (e.g. 14T). Therefore, the coil implantation shown here has further reduced this source of inhomogeneity and allowed for a consistent and stable shim. By implanting the coil on the surface of the skull, we can

achieve a significantly higher SNR which can be comparable to cryoprobe designs at close distances. This is even more so the case with the figure 8 coil shown here which gives a 5-times increase in SNR over the standard commercially available 4 array mouse head coil for 9.4T (both operating at room temperature) **(Figure 1**). This improvement allows much higher spatial resolution in awake mouse fMRI, at a two nanoliter voxel volume, compared to contemporary efforts in human brain mapping at sub-millimeter resolution (0.5-0.8mm isotropic), a difference of two orders of magnitude(81–84).

Brain-wide functional mapping with visual and vibrissa stimulation

There are fMRI studies investigating the visual system in both anesthetized and awake mice (55, 63, 85–88). In contrast to brain activation patterns at the VC, SC, and LGN(55), robust ACA activation was also detected for awake mouse fMRI in this study (**Fig 3**). Since ACA has been closely involved in pupil dynamics, as well as arousal state regulation(89–91), the mapping of the ACA in awake mice during visual stimulation provides a meaningful way to validate the conscious state of the mouse during scanning. Similarly, there are extensive rodent fMRI studies of vibrissa stimulation (44, 92–96). In contrast to the anesthetized state, this awake mouse fMRI detected not only activated contralateral BC and VPM, but also spread activation in the motor cortex, and small portion of the ipsilateral BC with positive BOLD signals. Although the air-puff stimulation was set and verified to deflect the whiskers of chosen side, videos of the mouse during scanning show that actively bilateral whisking could be initiated upon air-puff. This could lead to bilateral activation of the motor cortex and the ipsilateral BC. Furthermore, studies have been performed to understand the transcallosal activity-mediated excitatory/inhibitory circuits by both fMRI and optical imaging(79, 97–101). The potential transcallosal mediation of the negative BOLD signal detected in the superficial cortical area near BC will need to be further investigated. Also, negative BOLD signals were detected across a large brain area, which is consistent with astrocyte-mediated negative BOLD during brain state changes reported in anesthetized rats(29) and eye open/close-coupled arousal changes in unanesthetized monkeys(102). Interestingly, vibrissa stimulation also led to robust VRA activation in awake mice(103). VRA serves as one of the major nodes of default mode network (DMN) across different species(104–108). The vibrissa stimulation-evoked VRA activation suggests the higher-level cortical function contribute to vibrissa sensory processing in awake mice.

VRA-coupled pre-stimulus BC activation in awake mice as a sign of anticipation

There are extensive studies investigating brain activation responsible for anticipation with fMRI and electrophysiological recordings(109–113). In contrast to the reward anticipation or audiovisual anticipation of naturalistic music and movie clips that demand more complex cognitive processing(114–117), the repetitive air-puff stimulation delivered during head-fixed training for fMRI studies could serve as a simple paradigm to process the anticipatory responses in awake mice. Based on cross-correlation analysis with evoked VRA BOLD responses, the strongest correlation with the BC was detected from 6s lag-time based correlation maps, showing a positive BOLD signal at a time point 2 sec prior to stimulus onset (**Figure 5**). This anticipatory BC responses was not detected when the stimulation paradigm was randomized for air-puff stimulation in another group of mice. VRA is known to be involved in prediction(118–120) and has been coupled with temporal prediction in rodents(119, 121), as well as navigation efficiency involving spatial reference cues(119–121). Additionally, external somatosensory cues (e.g. the air puff or brushing of whiskers) are an important factor when investigating prediction processing(122–126). Previous work has shown that prediction of external stimulation will cause a hemodynamic response even in the absence of a stimulus(113, 127). In our study, we show that after continued regularly spaced stimulation, early somatosensory hemodynamic responses begin to have a significant impact seen in the averaged BOLD response time course. These anticipatory hemodynamic responses are a result of the continuous training for mice experiencing months of repetitive stimulation. The increased BOLD signal in the BC before the stimulus onset shows strong cross-correlation to the VRA activation, but VRA activation is not dependent on the pre-stimulus activation in the BC. This can be seen though the comparable VRA BOLD responses between repetitive and randomized air-puff stimulation paradigms (Fig 6C). This result indicates that VRA response mediates external sensory perception and may serve as a key association cortical area for the processing of the anticipated vibrissa signals but is not solely dependent on the prediction of incoming stimulus.

Methods

<u>Animals</u>

Thirty-five C57BL/6 mice were used in the current study (weighing between 20 and 30 g). Mice were group housed (3-4/cage) under a 12-h light/dark cycle with food and water ad libitum. All animal procedures were conducted in accordance with protocols approved by the Massachusetts General Hospital (MGH) Institutional Animal Care and Use Committee (IACUC), and animals were cared for according to the requirements of the National Research Council's Guide for the Care and Use of Laboratory Animals.

Awake mouse fMRI setup

The awake mouse cradle was designed in Blender and 3D printed using a Formlabs 3L 3D printer (Formlabs Inc., Somerville, MA). The design incorporated a sliding track which accepted the PCB chip transceiver circuit to slide in while the mouse was inserted into the cradle. Two transceiver circuit designs were built, a single loop and a figure 8 design. Each one keeps the B_1 direction orthogonal to the B_0. The single loop allows for full brain coverage at sufficient depths for subcortical investigation. The figure 8 design, due to its smaller coil loops and B_1 direction, is limited to precise measurements of shallow brain regions but provides a significant increase in SNR which is beneficial to cortical specific studies which do not have a need to look deeper into subcortical regions but would benefit from a much higher SNR. The single loop or Figure 8 shape RF coils were built to optimize tuning/matching performance when affixed onto the mouse skull. The coils serve to optimize the B_0 homogeneity by minimizing the air-tissue interface. Each coil was built to weigh ~2.5g to minimize the recovery/neck strengthening time of each mouse. The standardized RF coil was acquired from MRIBOT LLC (Malden, MA).

Animal Surgery

Mice underwent surgery to affix the RF coil to the head. Animals were anesthetized for surgery using isoflurane. Induction was accomplished using 5% isoflurane and 1L/min of medical air and 0.2L/min additional O_2 flow. Animals were maintained at 1.5%-2% isoflurane using respiration rate as a monitor for anesthesia depth. To attach the head coil, mice were affixed in a stereotaxic stage to stabilize the head with ear and bite bars. The scalp was shaved sterilized with ethanol and iodine and an incision was made to expose an area of the scull the size of the RF coil ring. The skull was cleaned of residual tissue and cleaned with 0.3% H_2O_2 and PBS before being dried. The coil was then positioned over the skull covering the underlying brain. The coil ring was

lifted ~0.3-0.5mm above the surface of the skull to avoid over-loading effects and held in place while a thin layer of cyanoacrylate glue was applied to connect the skull with the coil. Once dried (~5-8 mins), 2-part dental cement (Stoelting Co., Wood Dale, IL) was mixed and applied to cover the coil and exposed bone paying special note to the base of the coil to firmly secure it and avoid air bubbles and drips toward the eyes. The edges of the skin were then glued to close the surgical site. After the dental cement had fully hardened (~10 mins), the mouse was released from the stereotaxic stage and received subcutaneous injections of Dexamethasone and Cefazolin. Mice were then allowed to recover in their home cage for at least 1 week to ensure ample neck strengthening had occurred and the mice could walk with normal head posture.

Animal Training

To acclimate the animals to the MRI environment, intermittent habitual procedures were applied to train animals for 5 weeks before fMRI experiments. Training methods followed previous work(63) but modifying to a 5-week consecutive training period. Training time increased in the same fashion but increased as follows: 10min (Week 1), 20min (Week 2), 35min (Week 3), 45min (Week 4), 60min (Week 5).

Anesthesia Regiment for MRI measurements of SNR

While acquiring images to measure SNR improvements, all animals were anesthetized for the duration of MR scanning. Mice were induced using 5% isoflurane in medical air and maintained with 1.0-2.0% isoflurane, adjusted to retain stable physiological conditions while in the magnet. The gas mixture was supplied through the hollow bite bar directly to the mouth and nose of the animal at a rate of 1.0L/min. Animals were anesthetized to minimize artifacts associated with motion. Physiological monitoring of the animal was performed through the integration of a Small Animal Monitoring and Gating System (Model 1030, SA Instruments, Inc., Stony Brook, NY) capable of recording respiration, body temperature, electrocardiogram, and other parameters. The animal's breathing rate was continuously monitored and recorded during scanning using a pressure-sensitive sensor-pad and maintained between 50-80 breaths/min. Animals were kept at a constant temperature of 37°C in the MRI scanner by means of blowing warm air through the bore and recorded using a rectal thermometer probe.

MRI methods

^{1}H MRI data was acquired using the 14T and 9.4T horizontal MRI scanners (Magnex Sci, UK) located at the Athinoula A. Martinos Center for Biomedical Imaging in Boston, MA. The 14T magnet is equipped with a Bruker Avance Neo Console (Bruker-Biospin, Billerica, MA) and is operated using ParaVision 360 V.3.3. A microimaging gradient system (Resonance Research, Inc., Billerica, MA) provides a peak gradient strength of 1.2T/m over a 60-mm diameter. The 9.4T scanner is equipped with a Bruker Avance III HD Console (Bruker-Biospin, Billerica, MA) and is operated using ParaVision 6. A dual microimaging gradient system comprises a Bruker gradient coil capable of 44 G/cm, and a Resonance Research (Billerica, MA) gradient insert capable of 150 G/cm.

fMRI BOLD Imaging:

Multislice 2D gradient-echo Echo Planar Imaging (EPI) was used to acquire fMRI BOLD data from the awake animals with the following parameters: TE/TR = 7ms/1s, segments = 2, bandwidth = 277,777Hz, 100µm x 100µm in plane resolution with a 200µm slice thickness, 36 slices, 205 repetitions for an acquisition time of 6 minutes 50 seconds.

SNR Measurements:

^{1}H MRI data for SNR measurements were acquired on 9.4T (400MHz) and 14T (600MHZ) scanners using the following parameters for both systems: TE/TR = 3ms/475ms, flip angle = 30°, and 4 averages for an approximate acquisition time of 4.5 minutes.
9.4T scanner was only used to show SNR improvements from the implantable coils. The BOLD fMRI data were collected only at 14T due to the much-improved SNR available and were collected solely in awake mice to investigate signal associated with the awake functional connectivity.

Anatomical Imaging:

^{1}H MRI data for anatomical registration data were acquired using a multi-slice T_1-weighted 2D gradient echo Fast Low Angle SHot (FLASH) sequence with the same parameters of the SNR measurement scans except the resolution was adjusted to match the BOLD data at 100µm x 100µm x 200µm resolution.

Stimulation method/paradigm

The visual and vibrissa stimulation block paradigm was designed as follows: 5 baseline scans, 1 stimulation trigger scan, 19 inter-stimulation scans, and 10 epochs. The visual stimulation used 2 different wavelengths of light: 530nm and 490nm, which flashed at 5Hz and 5.1Hz, respectively, for 8 seconds with a 20ms "on" time of each illumination. The whisker air puff stimulation used the same block design as the visual stimulation but stimulated with a 10ms puff duration and an 8Hz firing rate for 8 seconds. Due to the use of 2 segments for these experiments, the effective TR was 2s. Therefore, the stimulation duration for both visual and vibrissa experiments resulted in 4 consecutive scans being included in the "on" stimulation period and 16 consecutive scans being included in the "rest" period. The random vibrissa stimulation paradigm used the same 10ms air puff at 8Hz for 8 seconds but randomized the "rest" duration. "Rest" durations were 12s, 22s, 32s, and 42s and randomized in 3 different sequences maintaining a scan duration of 205 TRs for each experiment.

Processing/Analysis methods (AFNI and MATLAB))

SNR was computed by dividing mean signal over the standard deviation of the noise. fMRI data was processed using Analysis of Functional Neuroimages (AFNI)(128, 129). Bruker 2dseq images of the EPI and FLASH scans were converted to AFNI format using 'to3d' before masking and aligning the dataset to a template.

To process the high resolution stimulated BOLD response from the visual and vibrissa stimulation paradigms, we developed a processing pipeline (**Supp Figure 1**). For each experiment, FLASH data were averaged for anatomical localization and the EPI scans were time averaged before registration. The time-averaged EPI was then registered to the FLASH and then to the Australian Mouse Brain Mapping Consortium (AMBMC) atlas(130) where a mask was generated. Each time series for each experiment was concatenated so each experiment contains one long time series dataset using the '3dTcat' command. Data were then despiked before each EPI time point was registered, via a 6-degree transformation, to the atlas using the 'volreg' command after which the previously generated mask was applied. The 'blur' command was used to smooth the newly transformed data before it was scaled and underwent a linear regression. All concatenated data was then split and summed, per each experimental study, to undergo motion correction and outlier removal. The corrected data was then summed and averaged with the remaining processed data to

generate a single time series across all experiments. A clustering threshold was set at 100 voxels and the Pearson correlation values were limited to $p \leq 0.01$ (corrected) with estimated false discover rate at $q=0.00078$. For the random stimulation design, the 3 runs were concatenated into a single time series each ensuring they all followed the same series of random timings.

Acknowledgements

The research benefited from funding from the NIH Brain Initiative grants (RF1NS113278, RF1NS124778, R01NS122904, R01NS120594, and R21NS121642), U19 Cooperative Agreement Grant (U19NS123717), S10 instrument grants (S10OD028616 and S10RR025563) to the Massachusetts General Hospital/Harvard-MIT Program in Health Sciences and Technology Martinos Center, and NSF CBET grant (2123970).

Figures and Legends

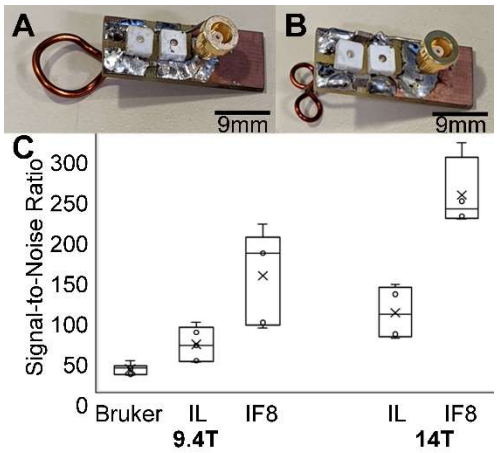

Figure 1. The comparison of SNR between implanted single loop (IL) and implanted figure 8 (IF8) RF coils and the commercial phase-array surface coil. **A**. The representative picture of the implantable single-loop RF coil. **B**. The representative picture of the figure 8 RF coil. **C.** The bar graph shows the SNR of anatomical images acquired with different RF coils using the 9.4T scanner ($\overline{SNR}_{Bruker} = 27.2, N = 6,\ \overline{SNR}_{IL} = 57.5, N = 5,\ \overline{SNR}_{IF} = 142.5, N = 5$) and the 14T scanner ($\overline{SNR}_{IL} = 96.8, N = 4,\ \overline{SNR}_{IF8} = 209.2, N = 5$).

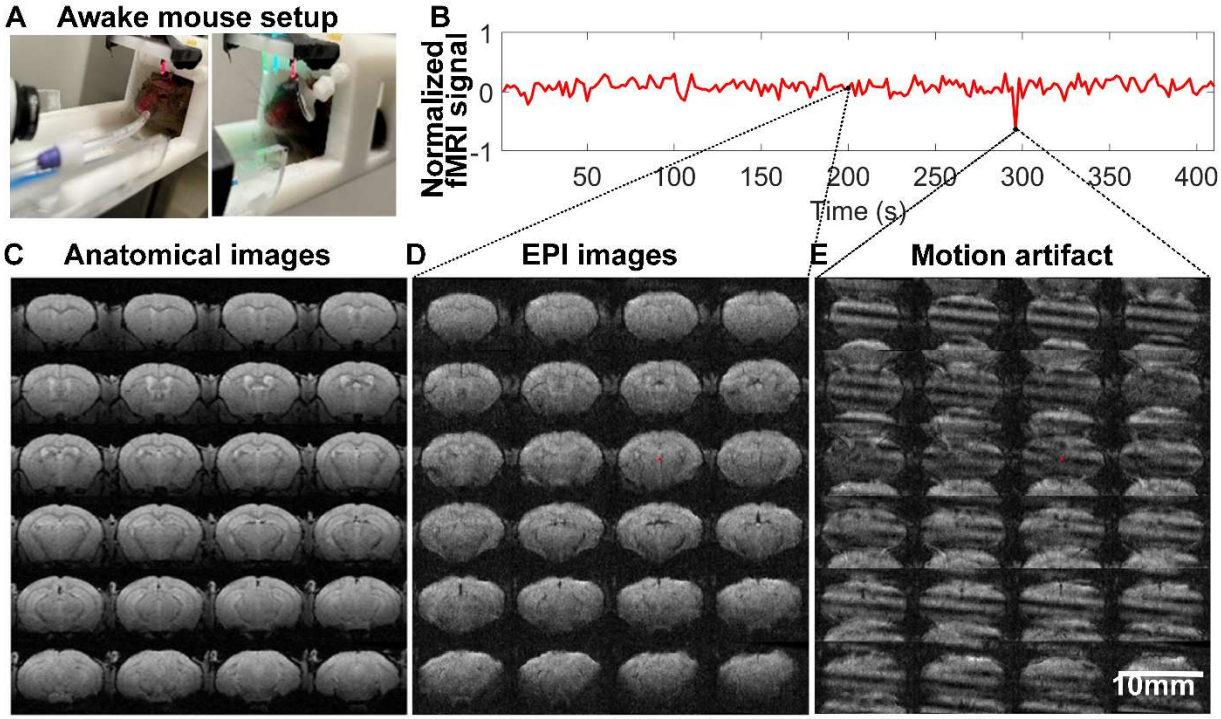

Figure 2. High resolution awake mouse fMRI at 14T. **A**. The awake mouse setup with head-fixed position in a customer-built cradle for visual and vibrissa stimulation. **B.** The representative fMRI

time course of an awake mouse based on raw image data acquired from high-resolution EPI, enabling the trace of motion-induced artifacts. **C**. The anatomical MRI images (FLASH) acquired from one representative awake mouse, showing minimal susceptibility and whole brain coverage from the implanted surface coil. **D**. The raw EPI fMRI image with same spatial resolution as the anatomical FLASH image. **E**. The snapshot of the distorted images due to motion of the awake mouse during scanning (Supplementary Movie 2 shows the video of motion-induced artifacts throughout the fMRI trial).

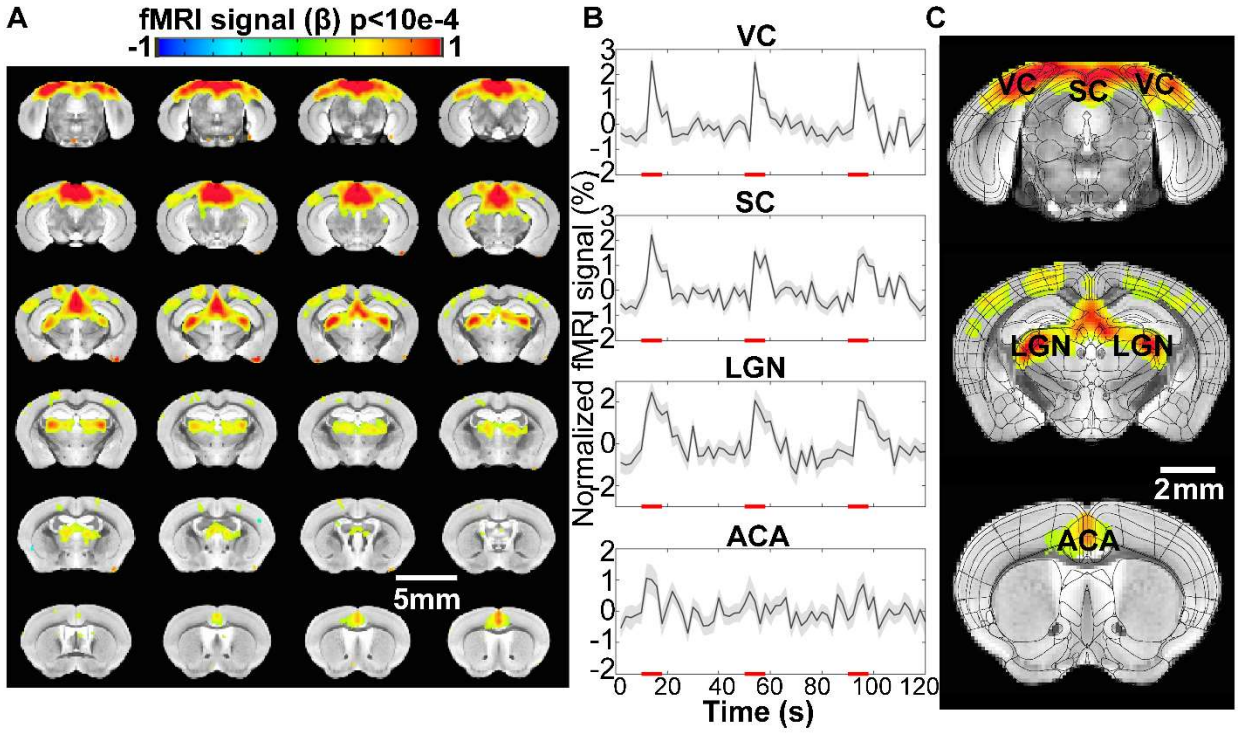

Figure 3. Visual stimulation-evoked high-resolution fMRI of awake mice. **A.** The brain-wide functional maps of awake mice show the strong positive BOLD activation in the visual cortex (VC), lateral geniculate nucleus (LGN), superior colliculus (SC), and anterior cingulate area (ACA)) based on the group analysis. **B.** The averaged time course of the ROIs based on brain atlas, demonstrating the evoked positive BOLD signal changes upon the 8s visual stimulation (5Hz 530nm and 5.1Hz 490nm 20ms light pluses). Each graph displays the average of 162 sets of 3 stimulation epochs. Shaded regions represent standard error. Red lines represent the 8s stimulation duration. **C.** The functional maps overlain with the brain atlas to highlight the activated brains regions: VC, SC, LGN, and ACA.

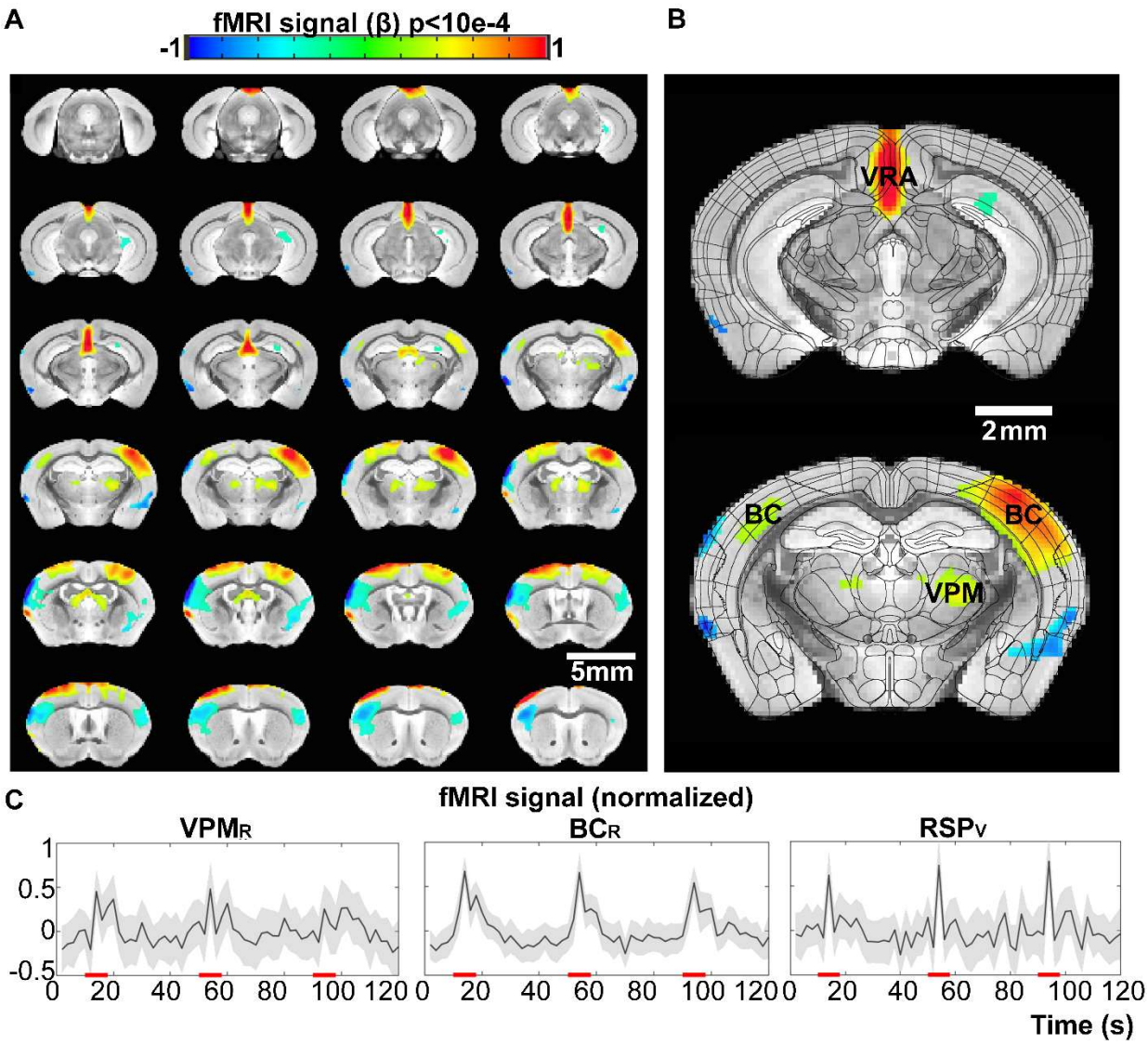

Figure 4. Vibrissa stimulation-evoked high-resolution fMRI of awake mice. **A**. The brain-wide functional maps of awake mice show the strong positive BOLD activation in the contralateral barrel cortex (BC) and ventral posteromedial nucleus (VPM) and posterior thalamic nucleus (PO). Positive BOLD signals are also detected at the motor cortex (MC) and the ventral retrosplenial area (VRA), as well as at the ipsilateral BC and thalamic nuclei. **B.** The functional maps are overlain with the brain atlas to highlight the activated vibrissa thalamocortical pathway (VPM→BC) and the VRA in awake mice. **C.** The averaged time course based on the brain atlas ROIs for VMP, BC, and VRA, demonstrating positive BOLD signal changes upon the 8s air-puff vibrissa stimulation (8Hz, 10ms). Each graph displays the average of 279 sets of 3 stimulation epochs. Shaded regions represent standard error. Red lines represent the 8s stimulation duration.

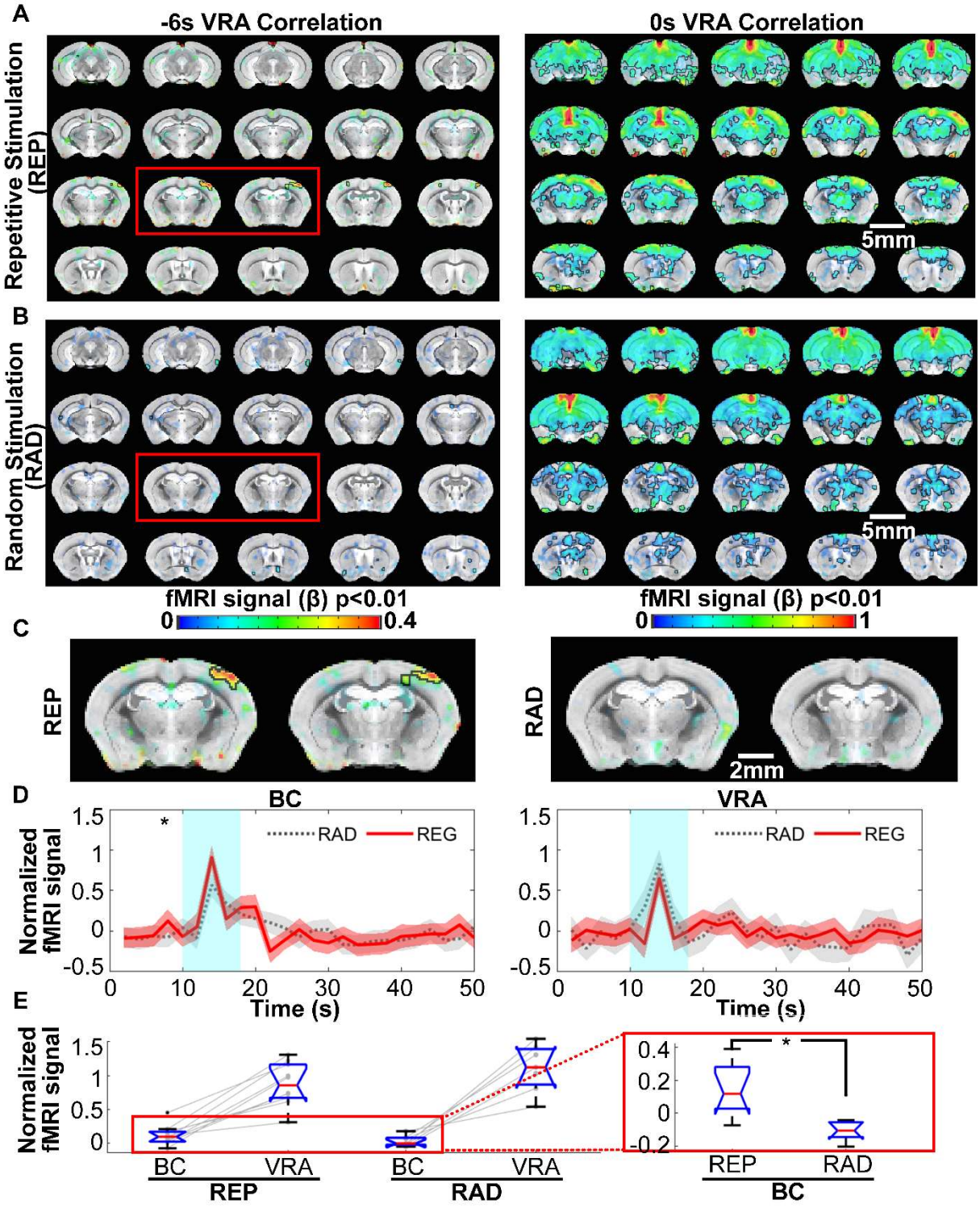

Figure 5. VRA-based brain-wide correlation maps at different time shifts. **A**. The VRA-based correlation maps at -6s and 0s time shifts of awake mice with repetitive stimulation (REP). The strong correlation in the contralateral BC is shown in the correlation map at the -6s time shift (red

box). **B**. The VRA-based correlation maps at -6s and 0s time shifts of awake mice with randomized stimulation (RAD). No correlation is detected in the contralateral BC at the -6s time shift (red box). **C.** The enlarged images from the -6s time shift correlation maps of REP and RAD groups, demonstrating the strong correlation patterns located at the contralateral BC only in the REP group. **D**. The averaged time course from both contralateral BC and VRA of REP and RAD groups, showing that early positive BOLD signals detected at 2 s prior to the stimulation in contralateral BC of the REP group and no significance difference detected in VRA. **E**. The bar graph presents the mean BOLD signals of contralateral BC at 2s prior to stimulation time point and peak signals of VRA in REP and RAD groups. The inset is the expanded bar graph to show the significantly higher BOLD signals detected in the contralateral BC at 2 s prior to stimulation in REP group ($p=0.015$, REP graph displays the average of 930 stimulation epochs, RAD graph displays the average of 240 stimulation epochs)

Supplementary materials and Figures

"High-resolution awake mouse fMRI at 14 Tesla" David Hike[1*], Xiaochen Liu[1*], Zeping Xie[1], Bei Zhang[1], Sangcheon Choi[1], Xiaoqing Alice Zhou[1], Andy Liu[1,2], Alyssa Murstein[1,2], Yuanyuan Jiang[1], Anna Devor[1,3], Xin Yu[1]

Supplementary Figures and Legends

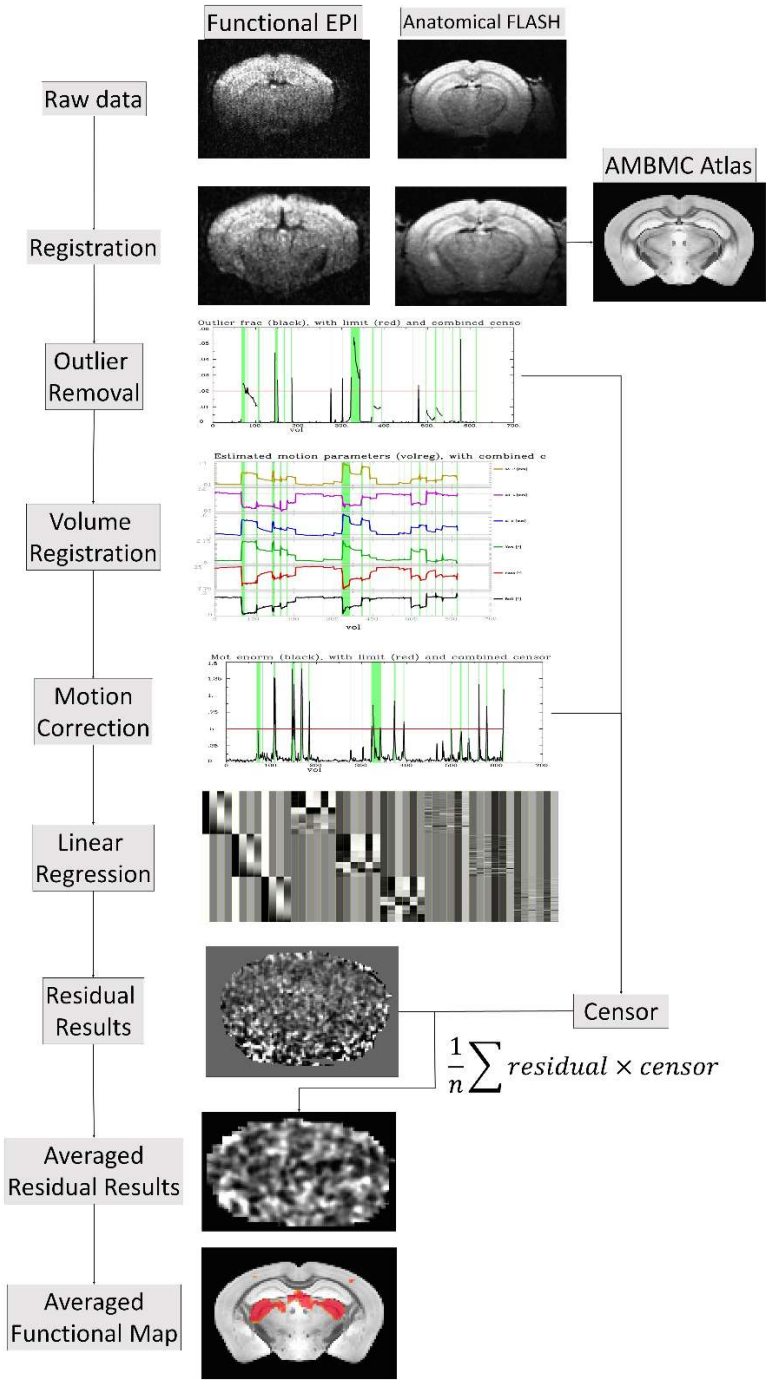

Supp Fig 1. The processing pipeline of the awake mouse fMRI datasets. The workflow diagram is described through the following steps: raw data registration, outlier removal, volume registration-based motion file estimation, Motion removal, linear regression with the censoring function, functional map demonstration.

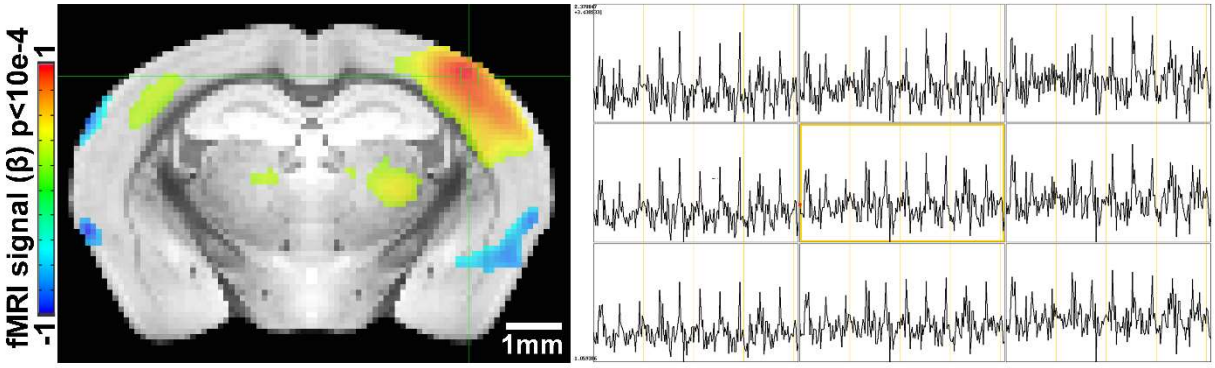

Supp Fig 2. The awake mouse fMRI with vibrissa stimulation. Left panel is the average functional map highlighting BOLD activation in the contralateral BC. Right panel is a 3x3 matrix presenting the time course data from the green box located in the barrel cortex. The positive BOLD signals can be well identified through the ten epoch on/off stimulation paradigm.

Supplementary Movie Legend

SuppMovie1.avi

Supp Movie 1. The video shows how awake mouse is set up through the cradle using the implanted RF coil.

SuppMovie2.avi

Supp Movie 2. The video shows the real-time EPI raw images from awake mice. The real-time tracer from the selected point demonstrates the time points with motion, as well as the motion-induced image distortion during awake mouse fMRI.

References

1. S. Ogawa, T. M. Lee, A. R. Kay, D. W. Tank, Brain magnetic resonance imaging with contrast dependent on blood oxygenation. *Proc Natl Acad Sci U S A* **87**, 9868–9872 (1990).
2. S. Ogawa, T. -M Lee, A. S. Nayak, P. Glynn, Oxygenation-sensitive contrast in magnetic resonance image of rodent brain at high magnetic fields. *Magn Reson Med* **14**, 68–78 (1990).
3. N. K. Logothetis, J. Pauls, M. Augath, T. Trinath, A. Oeltermann, Neurophysiological investigation of the basis of the fMRI signal. *Nature 2001 412:6843* **412**, 150–157 (2001).
4. L. Pauling, C. D. Coryell, The Magnetic Properties and Structure of Hemoglobin, Oxyhemoglobin and Carbonmonoxyhemoglobin. *Proc Natl Acad Sci U S A* **22**, 210 (1936).
5. S. Ogawa, *et al.*, Intrinsic signal changes accompanying sensory stimulation: functional brain mapping with magnetic resonance imaging. *Proc Natl Acad Sci U S A* **89**, 5951–5955 (1992).
6. K. K. Kwong, *et al.*, Dynamic magnetic resonance imaging of human brain activity during primary sensory stimulation. *Proc Natl Acad Sci U S A* **89**, 5675–5679 (1992).
7. P. A. Bandettini, E. C. Wong, R. S. Hinks, R. S. Tikofsky, J. S. Hyde, Time course EPI of human brain function during task activation. *Magn Reson Med* **25**, 390–397 (1992).
8. X. A. Zhou, Y. Jiang, W. Man, X. Yu, Multimodal methods to help interpret resting-state fMRI. *Advances in Resting-State Functional MRI: Methods, Interpretation, and Applications*, 207–235 (2023).
9. X. Yu, *et al.*, Sensory and optogenetically driven single-vessel fMRI. *Nature Methods 2016 13:4* **13**, 337–340 (2016).
10. K. Yoshida, *et al.*, Physiological effects of a habituation procedure for functional MRI in awake mice using a cryogenic radiofrequency probe. *J Neurosci Methods* **274**, 38–48 (2016).
11. L. Pérez-Cervera, *et al.*, Mapping functional connectivity in the rodent brain using electric-stimulation fMRI. *Methods in Molecular Biology* **1718**, 117–134 (2018).
12. T. Pirttimäki, *et al.*, Implantable RF-coil with multiple electrodes for long-term EEG-fMRI monitoring in rodents. *J Neurosci Methods* **274**, 154–163 (2016).

13. A. Arbabi, *et al.*, Multiple-mouse magnetic resonance imaging with cryogenic radiofrequency probes for evaluation of brain development. *Neuroimage* **252**, 119008 (2022).
14. A. Labbé, *et al.*, Recent Advances and Challenges in the Development of Radiofrequency HTS Coil for MRI. *Front Phys* **9**, 705438 (2021).
15. K. Masamoto, T. Kim, M. Fukuda, P. Wang, S. G. Kim, Relationship between neural, vascular, and BOLD signals in isoflurane-anesthetized rat somatosensory cortex. *Cereb Cortex* **17**, 942–950 (2007).
16. K. Kawazoe, *et al.*, Dose-dependent effects of esketamine on brain activity in awake mice: A BOLD phMRI study. *Pharmacol Res Perspect* **10**, e01035 (2022).
17. Q. Bukhari, A. Schroeter, M. Rudin, Increasing isoflurane dose reduces homotopic correlation and functional segregation of brain networks in mice as revealed by resting-state fMRI. *Sci Rep* **8** (2018).
18. A. R. Steiner, F. Rousseau-Blass, A. Schroeter, S. Hartnack, R. Bettschart-Wolfensberger, Systematic Review: Anesthetic Protocols and Management as Confounders in Rodent Blood Oxygen Level Dependent Functional Magnetic Resonance Imaging (BOLD fMRI)—Part B: Effects of Anesthetic Agents, Doses and Timing. *Animals 2021, Vol. 11, Page 199* **11**, 199 (2021).
19. H. J. Shim, *et al.*, Mouse fMRI under ketamine and xylazine anesthesia: Robust contralateral somatosensory cortex activation in response to forepaw stimulation. *Neuroimage* **177**, 30–44 (2018).
20. E. Jonckers, *et al.*, Different anesthesia regimes modulate the functional connectivity outcome in mice. *Magn Reson Med* **72**, 1103–1112 (2014).
21. T. Tsurugizawa, D. Yoshimaru, Impact of anesthesia on static and dynamic functional connectivity in mice. *Neuroimage* **241**, 118413 (2021).
22. Q. Bukhari, A. Schroeter, D. M. Cole, M. Rudin, Resting state fMRI in mice reveals anesthesia specific signatures of brain functional networks and their interactions. *Front Neural Circuits* **11**, 221781 (2017).
23. J. Grandjean, A. Schroeter, I. Batata, M. Rudin, Optimization of anesthesia protocol for resting-state fMRI in mice based on differential effects of anesthetics on functional connectivity patterns. *Neuroimage* **102**, 838–847 (2014).

24. G. J. P. C. Becq, E. L. Barbier, S. Achard, Brain networks of rats under anesthesia using resting-state fMRI: comparison with dead rats, random noise and generative models of networks. *J Neural Eng* **17**, 045012 (2020).
25. P. F. Conzen, *et al.*, Systemic and regional hemodynamics of isoflurane and sevoflurane in rats. *Anesth Analg* **74**, 79–88 (1992).
26. M. E. Magnuson, G. J. Thompson, W. J. Pan, S. D. Keilholz, Time-dependent effects of isoflurane and dexmedetomidine on functional connectivity, spectral characteristics, and spatial distribution of spontaneous BOLD fluctuations. *NMR Biomed* **27**, 291–303 (2014).
27. F. Zhao, T. Zhao, L. Zhou, Q. Wu, X. Hu, BOLD study of stimulation-induced neural activity and resting-state connectivity in medetomidine-sedated rat. *Neuroimage* **39**, 248–260 (2008).
28. X. Chen, *et al.*, Mapping optogenetically-driven single-vessel fMRI with concurrent neuronal calcium recordings in the rat hippocampus. *Nat Commun* **10** (2019).
29. M. Wang, Y. He, T. J. Sejnowski, X. Yu, Brain-state dependent astrocytic Ca2+ signals are coupled to both positive and negative BOLD-fMRI signals. *Proc Natl Acad Sci U S A* **115**, E1647–E1656 (2018).
30. W. B. Jung, G. H. Im, H. Jiang, S. G. Kim, Early fMRI responses to somatosensory and optogenetic stimulation reflect neural information flow. *Proc Natl Acad Sci U S A* **118**, e2023265118 (2021).
31. C. G. Cover, *et al.*, Whole brain dynamics during optogenetic self-stimulation of the medial prefrontal cortex in mice. *Commun Biol* **4** (2021).
32. F. Rocchi, *et al.*, Increased fMRI connectivity upon chemogenetic inhibition of the mouse prefrontal cortex. *Nature Communications 2022 13:1* **13**, 1–15 (2022).
33. J. Y. Lee, T. You, C. W. Woo, S. G. Kim, Optogenetic fMRI for Brain-Wide Circuit Analysis of Sensory Processing. *International Journal of Molecular Sciences 2022, Vol. 23, Page 12268* **23**, 12268 (2022).
34. V. Zerbi, *et al.*, Rapid Reconfiguration of the Functional Connectome after Chemogenetic Locus Coeruleus Activation. *Neuron* **103**, 702-718.e5 (2019).
35. A. Giorgi, *et al.*, Brain-wide Mapping of Endogenous Serotonergic Transmission via Chemogenetic fMRI. *Cell Rep* **21**, 910–918 (2017).

36. K. Schulz, *et al.*, Simultaneous BOLD fMRI and fiber-optic calcium recording in rat neocortex. *Nature Methods 2012 9:6* **9**, 597–602 (2012).
37. H.-I. Ioanas, *et al.*, Hybrid fiber optic-fMRI for multimodal cell-specific recording and manipulation of neural activity in rodents. *https://doi.org/10.1117/1.NPh.9.3.032206* **9**, 032206 (2022).
38. W. B. Jung, H. Jiang, S. Lee, S.-G. Kim, Dissection of brain-wide resting-state and functional somatosensory circuits by fMRI with optogenetic silencing https:/doi.org/10.1073/pnas.2113313119/-/DCSupplemental (November 8, 2023).
39. Y. Chen, P. Pais-Roldan, X. Chen, M. H. Frosz, X. Yu, MRI-guided robotic arm drives optogenetic fMRI with concurrent Ca2+ recording. *Nature Communications 2019 10:1* **10**, 1–11 (2019).
40. E. Dadgar-Kiani, J. H. Lee, Q. Liu, E. Dadgar-Kiani, Solving brain circuit function and dysfunction with computational modeling and optogenetic fMRI. *Science* **378**, 493–499 (2022).
41. Y. Nakamura, *et al.*, fMRI detects bilateral brain network activation following unilateral chemogenetic activation of direct striatal projection neurons. *Neuroimage* **220**, 117079 (2020).
42. L. M. Peeters, *et al.*, Chemogenetic silencing of neurons in the mouse anterior cingulate area modulates neuronal activity and functional connectivity. *Neuroimage* **220**, 117088 (2020).
43. E. A. Oyarzabal, *et al.*, Chemogenetic stimulation of tonic locus coeruleus activity strengthens the default mode network. *Sci Adv* **8**, 9898 (2022).
44. T. You, G. H. Im, S. G. Kim, Characterization of brain-wide somatosensory BOLD fMRI in mice under dexmedetomidine/isoflurane and ketamine/xylazine. *Scientific Reports 2021 11:1* **11**, 1–13 (2021).
45. E. M. R. Lake, *et al.*, Simultaneous cortex-wide fluorescence Ca2+ imaging and whole-brain fMRI. *Nat Methods* **17**, 1262–1271 (2020).
46. M. Desai, *et al.*, Mapping brain networks in awake mice using combined optical neural control and fMRI. *J Neurophysiol* **105**, 1393–1405 (2011).
47. X. Chen, *et al.*, Sensory evoked fMRI paradigms in awake mice. *Neuroimage* **204**, 116242 (2020).

48. P. S. Sharp, *et al.*, Comparison of stimulus-evoked cerebral hemodynamics in the awake mouse and under a novel anesthetic regime. *Scientific Reports 2015 5:1* **5**, 1–14 (2015).
49. L. A. Low, L. C. Bauer, B. A. Klaunberg, Comparing the Effects of Isoflurane and Alpha Chloralose upon Mouse Physiology. *PLoS One* **11**, e0154936 (2016).
50. S. Gargiulo, *et al.*, Mice Anesthesia, Analgesia, and Care, Part II: Anesthetic Considerations in Preclinical Imaging Studies. *ILAR J* **53**, E70–E81 (2012).
51. M. S. Scheller, A. Tateishi, J. C. Drummond, M. H. Zornow, The effects of sevoflurane on cerebral blood flow, cerebral metabolic rate for oxygen, intracranial pressure, and the electroencephalogram are similar to those of isoflurane in the rabbit. *Anesthesiology* **68**, 548–551 (1988).
52. M. W. Crawford, J. Lerman, V. Saldivia, F. J. Carmichael, Hemodynamic and organ blood flow responses to halothane and sevoflurane anesthesia during spontaneous ventilation. *Anesth Analg* **75**, 1000–1006 (1992).
53. A. P. Harris, *et al.*, Imaging learned fear circuitry in awake mice using fMRI. *European Journal of Neuroscience* **42**, 2125–2134 (2015).
54. D. Gutierrez-Barragan, *et al.*, Unique spatiotemporal fMRI dynamics in the awake mouse brain. *Current Biology* **32**, 631-644.e6 (2022).
55. T. N. A. Dinh, W. B. Jung, H. J. Shim, S. G. Kim, Characteristics of fMRI responses to visual stimulation in anesthetized vs. awake mice. *Neuroimage* **226**, 117542 (2021).
56. Z. Han, *et al.*, Awake and behaving mouse fMRI during Go/No-Go task. *Neuroimage* **188**, 733–742 (2019).
57. M. Desjardins, *et al.*, Awake Mouse Imaging: From Two-Photon Microscopy to Blood Oxygen Level–Dependent Functional Magnetic Resonance Imaging. *Biol Psychiatry Cogn Neurosci Neuroimaging* **4**, 533–542 (2019).
58. D. Madularu, *et al.*, A non-invasive restraining system for awake mouse imaging. *J Neurosci Methods* **287**, 53–57 (2017).
59. K. Moore, *et al.*, BOLD Imaging in Awake Wild-Type and Mu-Opioid Receptor Knock-Out Mice Reveals On-Target Activation Maps in Response to Oxycodone. *Front Neurosci* **10** (2016).
60. W. Xu, *et al.*, A systematically optimized awake mouse fMRI paradigm. *bioRxiv*, 2022.11.16.516376 (2022).

61. Y. Liu, *et al.*, An open database of resting-state fMRI in awake rats. *Neuroimage* **220**, 117094 (2020).
62. J. Almeida, F. Severo, D. Nunes, Impact of the Sound of Magnetic Resonance Imaging Pulse Sequences in Awake Mice. *Journal of Applied Animal Welfare Science* **25**, 75–88 (2022).
63. H. Zeng, Y. Jiang, S. Beer-Hammer, X. Yu, Awake Mouse fMRI and Pupillary Recordings in the Ultra-High Magnetic Field. *Front Neurosci* **16**, 886709 (2022).
64. L. A. Low, L. C. Bauer, M. H. Pitcher, M. C. Bushnell, Restraint training for awake functional brain scanning of rodents can cause long-lasting changes in pain and stress responses. *Pain* **157**, 1761–1772 (2016).
65. S. Chiba, *et al.*, Chronic restraint stress causes anxiety- and depression-like behaviors, downregulates glucocorticoid receptor expression, and attenuates glutamate release induced by brain-derived neurotrophic factor in the prefrontal cortex. *Prog Neuropsychopharmacol Biol Psychiatry* **39**, 112–119 (2012).
66. E. A. Ferenczi, *et al.*, Prefrontal cortical regulation of brainwide circuit dynamics and reward-related behavior. *Science* **351**, aac9698 (2016).
67. C. Baltes, N. Radzwill, S. Bosshard, D. Marek, M. Rudin, Micro MRI of the mouse brain using a novel 400 MHz cryogenic quadrature RF probe. *NMR Biomed* **22**, 834–842 (2009).
68. A. C. Wright, H. K. Song, F. W. Wehrli, In Vivo MR Micro Imaging With Conventional Radiofrequency Coils Cooled to 77°K. *Magn Reson Med* **43**, 163–169 (2000).
69. W. E. Kwok, Z. You, In vivo MRI using liquid nitrogen cooled phased array coil at 3.0 T. *Magn Reson Imaging* **24**, 819 (2006).
70. N. Takata, *et al.*, Optogenetic Activation of CA1 Pyramidal Neurons at the Dorsal and Ventral Hippocampus Evokes Distinct Brain-Wide Responses Revealed by Mouse fMRI. *PLoS One* **10** (2015).
71. Y. Abe, *et al.*, Optical manipulation of local cerebral blood flow in the deep brain of freely moving mice. *Cell Rep* **36** (2021).
72. H. T. Hamada, *et al.*, Optogenetic activation of dorsal raphe serotonin neurons induces a brain-wide response in reward network https:/doi.org/10.1101/2022.08.07.503074 (September 25, 2023).

73. T. H. R. Farmer, G. P. Cofer, G. A. Johnson, Maximizing contrast to noise with inductively coupled implanted coils. *Invest Radiol* **25**, 552–557 (1990).

74. R. M. Summers, *et al.*, MR microscopy of the rat carotid artery after balloon injury by using an implanted imaging coil. *Magn Reson Med* **33**, 785–789 (1995).

75. N. K. Logothetis, H. Merkle, M. Augath, T. Trinath, K. Uğurbil, Ultra High-Resolution fMRI in Monkeys with Implanted RF Coils. *Neuron* **35**, 227–242 (2002).

76. R. Wang, C. M. Dong, E. X. Wu, R. C. Roberts, L. J. Jiang, Circuitry design and magnetic susceptibility evaluation of 7T fMRI implantable RF coil. *2018 International Applied Computational Electromagnetics Society Symposium in Denver, ACES-Denver 2018* (2018) https:/doi.org/10.23919/ROPACES.2018.8364248 (August 13, 2023).

77. G. Lee, *et al.*, Implantable, Bioresorbable Radio Frequency Resonant Circuits for Magnetic Resonance Imaging. *Advanced Science*, 2301232 (2023).

78. D. Madularu, *et al.*, A chronic in situ coil system adapted for intracerebral stimulation during MRI in rats. *J Neurosci Methods* **284**, 85–95 (2017).

79. Y. Chen, *et al.*, Focal fMRI signal enhancement with implantable inductively coupled detectors. *Neuroimage* **247**, 118793 (2022).

80. R. Pohmann, O. Speck, K. Scheffler, Signal-to-noise ratio and MR tissue parameters in human brain imaging at 3, 7, and 9.4 tesla using current receive coil arrays. *Magn Reson Med* **75**, 801–809 (2016).

81. D. Haenelt, *et al.*, High-resolution quantitative and functional MRI indicate lower myelination of thin and thick stripes in human secondary visual cortex. *Elife* **12** (2023).

82. R. M. Heidemann, *et al.*, Isotropic submillimeter fMRI in the human brain at 7 T: Combining reduced field-of-view imaging and partially parallel acquisitions. *Magn Reson Med* **68**, 1506–1516 (2012).

83. E. Margalit, *et al.*, Ultra-high-resolution fMRI of Human Ventral Temporal Cortex Reveals Differential Representation of Categories and Domains. *Journal of Neuroscience* **40**, 3008–3024 (2020).

84. D. A. Feinberg, N. Cvetesic, A. Beckett, Pushing the limits of ultra-high resolution human brain imaging with SMS-EPI demonstrated for columnar level fMRI. *Neuroimage* **164**, 155 (2018).

85. W. Huang, *et al.*, Magnetic resonance imaging (MRI) detection of the murine brain response to light: temporal differentiation and negative functional MRI changes. *Proceedings of the National Academy of Sciences* **93**, 6037–6042 (1996).

86. H. L. Lee, Z. Li, E. J. Coulson, K. H. Chuang, Ultrafast fMRI of the rodent brain using simultaneous multi-slice EPI. *Neuroimage* **195**, 48–58 (2019).

87. A. Niranjan, I. N. Christie, S. G. Solomon, J. A. Wells, M. F. Lythgoe, fMRI mapping of the visual system in the mouse brain with interleaved snapshot GE-EPI. *Neuroimage* **139**, 337–345 (2016).

88. R. Lungu, F. F. Fernandes, T. F. Outeiro, N. Shemesh, Brain-wide sensory aberrations in a Parkinson's Disease mouse model revealed by functional MRI. *bioRxiv*, 2022.04.06.487227 (2022).

89. R. Becket Ebitz, M. L. Platt, Neuronal Activity in Primate Dorsal Anterior Cingulate Cortex Signals Task Conflict and Predicts Adjustments in Pupil-Linked Arousal (2015) https:/doi.org/10.1016/j.neuron.2014.12.053 (November 9, 2023).

90. S. Joshi, Y. Li, R. M. Kalwani, J. I. Gold, Relationships between Pupil Diameter and Neuronal Activity in the Locus Coeruleus, Colliculi, and Cingulate Cortex. *Neuron* **89**, 221–234 (2016).

91. T. Pfeffer, *et al.*, Coupling of pupil- and neuronal population dynamics reveals diverse influences of arousal on cortical processing. *Elife* **11** (2022).

92. N. Van der Knaap, D. Wiedermann, D. Schubert, M. Hoehn, J. R. Homberg, Perinatal SSRI exposure affects brain functional activity associated with whisker stimulation in adolescent and adult rats. *Scientific Reports 2021 11:1* **11**, 1–9 (2021).

93. H. Lu, *et al.*, Spatial correlations of laminar BOLD and CBV responses to rat whisker stimulation with neuronal activity localized by Fos expression. *Magn Reson Med* **52**, 1060–1068 (2004).

94. L. Balasco, *et al.*, Abnormal whisker-dependent behaviors and altered cortico-hippocampal connectivity in Shank3b−/− mice. *Cerebral Cortex* **32**, 3042–3056 (2022).

95. J. Ferrier, E. Tiran, T. Deffieux, M. Tanter, Z. Lenkei, Functional imaging evidence for task-induced deactivation and disconnection of a major default mode network hub in the mouse brain. *Proc Natl Acad Sci U S A* **117**, 15270–15280 (2020).

96. S.-H. Choi, *et al.*, No Replication of Direct Neuronal Activity-related (DIANA) fMRI in Anesthetized Mice. *bioRxiv*, 2023.05.26.542419 (2023).

97. H. J. Shim, J. Lee, S. G. Kim, BOLD fMRI and hemodynamic responses to somatosensory stimulation in anesthetized mice: spontaneous breathing vs. mechanical ventilation. *NMR Biomed* **33**, e4311 (2020).

98. S. Fujita, *et al.*, Spatiotemporal profiles of transcallosal connections in rat insular cortex revealed by in vivo optical imaging. *Neuroscience* **206**, 201–211 (2012).

99. C. Grefkes, S. B. Eickhoff, D. A. Nowak, M. Dafotakis, G. R. Fink, Dynamic intra- and interhemispheric interactions during unilateral and bilateral hand movements assessed with fMRI and DCM. *Neuroimage* **41**, 1382–1394 (2008).

100. D. Lenzi, *et al.*, Effect of corpus callosum damage on ipsilateral motor activation in patients with multiple sclerosis: A functional and anatomical study. *Hum Brain Mapp* **28**, 636 (2007).

101. M. Reddy, *et al.*, An fMRI study of the lateralization of motor cortex activation in acallosal patients. *Neuroreport* **11**, 2409–2413 (2000).

102. C. Chang, *et al.*, Tracking brain arousal fluctuations with fMRI. *Proc Natl Acad Sci U S A* **113**, 4518–4523 (2016).

103. A. Radwanska, *et al.*, Involvement of retrosplenial cortex in classical conditioning. *Behavioural Brain Research* **214**, 231–239 (2010).

104. H. Lu, *et al.*, Rat brains also have a default mode network. *Proc Natl Acad Sci U S A* **109**, 3979–3984 (2012).

105. J. R. Andrews-Hanna, J. S. Reidler, J. Sepulcre, R. Poulin, R. L. Buckner, Functional-Anatomic Fractionation of the Brain's Default Network. *Neuron* **65**, 550 (2010).

106. J. L. Vincent, *et al.*, Intrinsic functional architecture in the anaesthetized monkey brain. *Nature 2007 447:7140* **447**, 83–86 (2007).

107. J. K. Rilling, *et al.*, A comparison of resting-state brain activity in humans and chimpanzees. *Proc Natl Acad Sci U S A* **104**, 17146–17151 (2007).

108. M. E. Raichle, *et al.*, A default mode of brain function. *Proc Natl Acad Sci U S A* **98**, 676–682 (2001).

109. C. Zhao, *et al.*, Anticipatory alpha oscillation predicts attentional selection and hemodynamic response. *Hum Brain Mapp* **40**, 3606–3619 (2019).

110. L. E. Martin, G. F. Potts, P. C. Burton, P. R. Montague, Electrophysiological and Hemodynamic Responses to Reward Prediction Violation. *Neuroreport* **20**, 1140 (2009).

111. C. Zhao, *et al.*, The neurovascular couplings between electrophysiological and hemodynamic activities in anticipatory selective attention. *Cerebral Cortex* **32**, 4953–4968 (2022).

112. A. Ploghaus, L. Becerra, C. Borras, D. Borsook, Neural circuitry underlying pain modulation: Expectation, hypnosis, placebo. *Trends Cogn Sci* **7**, 197–200 (2003).

113. Y. B. Sirotin, A. Das, Anticipatory haemodynamic signals in sensory cortex not predicted by local neuronal activity. *Nature 2009 457:7228* **457**, 475–479 (2009).

114. G. Pezzulo, J. Hoffmann, R. Falcone, Anticipation and anticipatory behavior. *Cogn Process* **8**, 67–70 (2007).

115. A. P. McRobert, P. Ward, D. W. Eccles, A. M. Williams, The effect of manipulating context-specific information on perceptual–cognitive processes during a simulated anticipation task. *British Journal of Psychology* **102**, 519–534 (2011).

116. B. G. Burton, V. Hok, E. Save, B. Poucet, Lesion of the ventral and intermediate hippocampus abolishes anticipatory activity in the medial prefrontal cortex of the rat. *Behavioural Brain Research* **199**, 222–234 (2009).

117. K. T. Ciesielski, *et al.*, Role of medial cortical networks for anticipatory processing in obsessive-compulsive disorder. *Hum Brain Mapp* **33**, 2125–2134 (2012).

118. D. M. Smith, A. M. P. Miller, L. C. Vedder, The retrosplenial cortical role in encoding behaviorally significant cues. *Behavioral Neuroscience* **132**, 356–365 (2018).

119. A. M. P. Miller, W. Mau, D. M. Smith, Retrosplenial Cortical Representations of Space and Future Goal Locations Develop with Learning Correspondence. *Current Biology* **29** (2019).

120. S. D. Auger, E. A. Maguire, Assessing the mechanism of response in the retrosplenial cortex of good and poor navigators. *Cortex* **49**, 2904–2913 (2013).

121. J. M. Wyass, T. Van Groen, Connections between the retrosplenial cortex and the hippocampal formation in the rat: A review. *Hippocampus* **2**, 1–11 (1992).

122. J. S. Taube, The Head Direction Signal: Origins and Sensory-Motor Integration. *https://doi.org/10.1146/annurev.neuro.29.051605.112854* **30**, 181–207 (2007).

123. S. Valerio, J. S. Taube, Path integration: how the head direction signal maintains and corrects spatial orientation. *Nature Neuroscience 2012 15:10* **15**, 1445–1453 (2012).

124. T. P. Todd, D. I. Fournier, D. J. Bucci, Retrosplenial cortex and its role in cue-specific learning and memory. *Neurosci Biobehav Rev* **107**, 713–728 (2019).

125. B. G. Cooper, T. F. Manka, S. J. Y. Mizumori, Finding your way in the dark: The retrosplenial cortex contributes to spatial memory and navigation without visual cues. *Behavioral Neuroscience* **115**, 1012–1028 (2001).

126. C. S. Keene, D. J. Bucci, Contributions of the Retrosplenial and Posterior Parietal Cortices to Cue-Specific and Contextual Fear Conditioning. *Behavioral Neuroscience* **135**, 693–701 (2021).

127. Y. Yu, *et al.*, Layer-specific activation of sensory input and predictive feedback in the human primary somatosensory cortex. *Sci Adv* **5** (2019).

128. R. W. Cox, AFNI: Software for analysis and visualization of functional magnetic resonance neuroimages. *Computers and Biomedical Research* **29**, 162–173 (1996).

129. R. W. Cox, J. S. Hyde, Software tools for analysis and visualization of fMRI data. *NMR Biomed* **10**, 171–8 (1997).

130. A. L. Janke, J. F. P. Ullmann, Robust methods to create ex vivo minimum deformation atlases for brain mapping. *Methods* **73**, 18–26 (2015).